Bricked subwavelengh gratings: A tailorable biaxial on-chip metamaterial topology

José Manuel Luque González,[1] Alejandro Ortega-Moñux,[1] Robert Halir,[1,2] Jens H. Schmid,[3] Pavel Cheben,[3,4,*] Íñigo Molina-Fernández[1,2] and J. Gonzalo Wangüemert-Pérez[1,*]

[1]*Universidad de Málaga, Departamento de Ingeniería de Comunicaciones, ETSI Telecomunicación, Campus de Teatinos, 29071 Málaga, Spain*
[2]*Bionand Center for Nanomedicine and Biotechnology, Parque Tecnológico de Andalucía, 29590 Málaga, Spain*
[3]*National Research Council Canada, 1200 Montreal Road, Bldg. M50, Ottawa K1A 0R6, Canada*
[4]*Center for Research in Photonics, University of Ottawa, Ottawa K1N6N5, Canada*
**Corresponding authors:* pavel.cheben@nrc-cnrc.gc.ca and gonzalo@ic.uma.es

Integrated metamaterials are redefining the capabilities of silicon photonic chips. In providing lithographic control over dielectric permittivity, dispersion and anisotropy, they are enabling photonic devices with unprecedented performance. However, the implementation of these materials at telecom wavelengths often requires a fabrication resolution of the order of 100 nm and below, pushing current wafer-scale fabrication technology to its limits and hindering the widespread exploitation of on-chip metamaterials. Here we propose, for the first time, a subwavelength grating metamaterial with bricked topology, that provides lithographic control over the metamaterial dispersion and anisotropy using a single etch Manhattan-like geometry with pixel dimensions up to 150×150 nm^2, thereby opening a new path towards fabrication at wafer-scale. We analytically show that these structures effectively behave as biaxial crystals and validate their use in high performance on-chip beam-splitters. Through engineering of the metamaterial anisotropy tensor, the splitters are shown to exhibit sub-decibel insertion losses and imbalance over a 400 nm design bandwidth, via 3D FDTD simulations. We experimentally demonstrate an excellent device performance in a 140 nm bandwidth, limited by our measurement setup.

Driven by high quality lithography and dense optical integration, silicon photonics is enabling key advances in diverse areas including high speed optical communications[1], quantum technologies[2,3], artificial intelligence[4,5], supercomputing[6,7], lidars[8], spectroscopy[9] or sensing[10]. For these developments, preserving CMOS compatibility is crucial in order to leverage existing microelectronics fabrication infrastructure to mass produce silicon photonic chips[11,12]. Since there are only a few fully CMOS compatible materials, the design space is largely restricted in terms of the available optical properties, and this ultimately limits device performance. Dielectric on-chip metamaterials, originally introduced to address the light coupling bottleneck in silicon photonics[13,14], have the potential to overcome this limitation: By periodically patterning waveguides at the subwavelength scale, a wide range of equivalent refractive indexes can be synthesized lithographically on a chip[15–18]. What is more, with the ability to engineer dispersion and anisotropy these metamaterials are enabling completely new design strategies yielding devices with unprecedented performance, including ultra-broadband nanophotonic components[19,20], metalenses[21–23], densely spaced waveguides[24], polarization management devices[25–29], low crosstalk bends[30], or high sensitivity waveguide sensors[31,32]. However, to avoid Bragg resonances, subwavelength metamaterials often require fabrication resolutions of 100 nm and below at telecom wavelengths. While narrow single-mode interconnecting waveguides can operate with larger periods, for more sophisticated devices implemented in planar waveguides subwavelength structures can be prohibitively small to fabricate with wafer-scale lithography techniques. Advanced optical proximity correction[33] (OPC) can alleviate this issue for some device geometries. However, when control over material anisotropy is required, the structures that have so far been explored for this purpose (tilted, non-Manhattan patterns)[34] are not amenable to current OPC techniques. Therefore, it is currently not possible to exploit the full potential of metamaterials within an accessible silicon photonics fabrication process compatible with mass production. This limitation poses a serious obstacle to the use of high-performance metamaterial designs in silicon photonic devices.

To overcome this limitation, here we propose the bricked subwavelength grating, shown in Fig. 1(a), a new nanopatterning for on-chip metamaterials, which synthesizes a tailorable biaxial crystal with lithographic control over anisotropy and dispersion. This is achieved with a single etch step Manhattan-like geometry with a uniform grid and pixel dimensions up to 150×150 nm^2 for telecom wavelengths, thereby paving the way towards wafer-scale fabrication. We validate the properties of the material by designing on-chip beam-splitters with large pixel dimensions that cover bandwidths in excess of 400 nm at telecom wavelength with sub-decibel insertion losses and imbalance. These results are experimentally demonstrated in a 140 nm bandwidth, which is limited by the measurement setup.

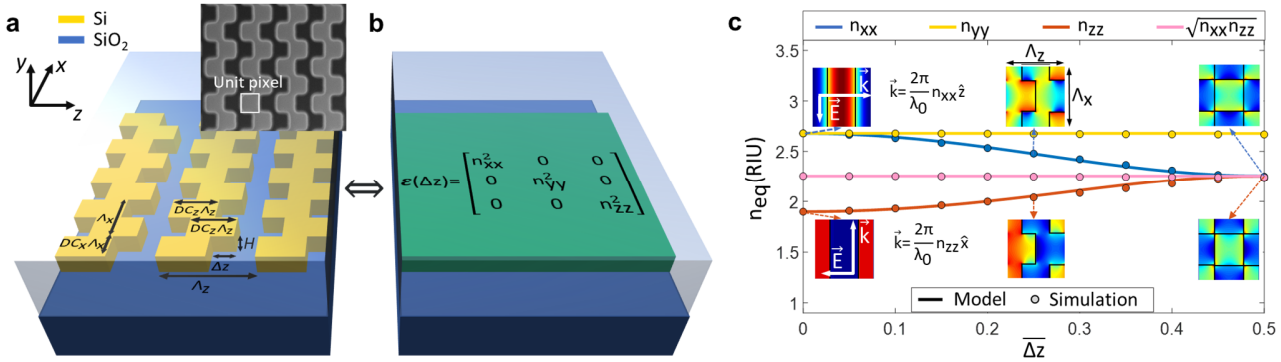

Fig. 1 (a) 3D-Schematic of a bricked SWG waveguide. The structure is formed by periodically partitioning the silicon segments of an SWG waveguide in the transverse direction (*x*-axis) alternately shifting the resulting blocks a length Δz. The silicon dioxide cladding is represented translucently. Inset: Scanning electron microscope (SEM) image of a fabricated bricked SWG structure, schematically showing a unit pixel. (b) Anisotropic homogenization of the bricked SWG core shown in (a) as a metamaterial defined by its diagonal permittivity tensor $\boldsymbol{\varepsilon}(\Delta z) = \mathrm{diag}[n_{xx}^2, n_{yy}^2, n_{zz}^2]$. (c) The tensor components of the synthesized metamaterial are lithography tailored by the shift Δz, providing control over the properties of the synthesized metamaterial without changing the duty-cycle. The insets show the electric field distribution, for polarization along the *z*- and *x*-axis, propagating in the *x* and *z* directions, respectively, as the shifting is increased. The normalized shift is defined as $\overline{\Delta z} = \Delta z/\Lambda_z$.

Results

Foundations of the bricked SWG metamaterial. A conventional subwavelength grating (SWG) waveguide comprises alternating strips of the core and the cladding materials, arrayed with a subwavelength period Λ_z along the propagation direction (*z*-axis). Referring to Fig. 1(a), in a bricked SWG waveguide, the silicon strips are periodically partitioned along the *x*-axis with a pitch Λ_x, and the resulting silicon blocks are then alternately shifted by a distance Δz in the *z*-direction. We refer to the duty-cycles in the *x* and *z* directions as DC_x and DC_z, respectively, setting them advantageously to 50% as this yields the largest pixel dimensions.

To obtain an analytical model of this metamaterial we will consider a simplified structure that extends the bricked SWG medium infinitely along the *x*-axis and the *y*-axis, with light propagating in the *x*-*z* plane. For the purpose of illustration, we will consider a central wavelength of $\lambda_0 = 1.55$ μm, with material refractive indices $n_{\mathrm{Si}} = 3.476$ and $n_{\mathrm{SiO_2}} = 1.444$ and $\mathrm{DC_x} = \mathrm{DC_z} = 50\%$. At this point of the analysis we assume operation in the deep subwavelength regime, i.e. $\Lambda \ll \lambda_0$, as this simplifies mathematical model – in the next section we show that the key predictions of this model remain valid for longer subwavelength periods. Based on our previous works[19,22,34], we model the periodic structure as a homogeneous anisotropic medium, described by its permittivity tensor $\boldsymbol{\varepsilon}(\overline{\Delta z})$:

$$\boldsymbol{\varepsilon}(\overline{\Delta z}) = \begin{bmatrix} n_{xx}^2(\overline{\Delta z}) & 0 \\ 0 & n_{zz}^2(\overline{\Delta z}) \end{bmatrix}, \qquad (1)$$

where $\overline{\Delta z} = \Delta z/\Lambda_z$. The n_{yy}^2 component of the permittivity tensor has been omitted because this component is independent of the block shifting, as will be demonstrated later in our analysis. We first consider the boundary case $\Delta z = 0$, that is, a conventional SWG structure, for which the index tensor is given by: $n_{xx}(0) = n_{\parallel}$ and $n_{zz}(0) = n_{\perp}$, with $n_{\parallel}$ and $n_{\perp}$ being the equivalent refractive indices for polarization parallel and perpendicular to the interfaces between the interleaved materials – see insets in Fig. 1(c). The permittivity tensor in this case is thus given by $\boldsymbol{\varepsilon}(0) = \mathrm{diag}[n_{\parallel}^2, n_{\perp}^2]$. The constants $n_{\parallel}$ and $n_{\perp}$ can be analytically calculated using different approaches[35,36], with the well-known Rytov formulas yielding $n_{\parallel} = (\mathrm{DC}_z n_{\mathrm{Si}}^2 + (1-\mathrm{DC})n_{\mathrm{SiO_2}}^{-2})^{1/2} = 2.66$ and $n_{\perp} = \left(\mathrm{DC}_z n_{\mathrm{Si}}^{-2} + (1-\mathrm{DC}_z)n_{\mathrm{SiO_2}}^{-2}\right)^{-1/2} = 1.89$. Let's now consider a second a boundary case, $\overline{\Delta z} = 0.5$, yiedling a chequerboard type structure – see insets in Fig. 1(c). Assuming a 50% duty cycle in both *x* and *z* directions, the symmetry of this configuration implies that light propagation is invariant along the *x* and *z* axes, that is, $n_{xx}(0.5) = n_{zz}(0.5)$. To calculate the component values in this case we use the index conservation law[37]. The latter implies that for a diagonal permittivity tensor the determinant, $\det|\boldsymbol{\varepsilon}(\overline{\Delta z})|$, is invariant on the shift $\overline{\Delta z}$, resulting in the following relation between the refractive index components:

$$\det|\boldsymbol{\varepsilon}(\overline{\Delta z})| = n_{xx}^2(\overline{\Delta z}) \cdot n_{zz}^2(\overline{\Delta z}) = \det|\boldsymbol{\varepsilon}(0)| = n_{\parallel}^2 n_{\perp}^2. \qquad (2)$$

Using this equation, we can calculate the permittivity tensor for the chequerboard geometry, obtaining $\boldsymbol{\varepsilon}(0.5) = \mathrm{diag}[n_{\parallel}n_{\perp}, n_{\parallel}n_{\perp}]$. So far, we have calculated the permittivity tensor for the boundary cases, $\overline{\Delta z} = 0$ and $\overline{\Delta z} = 0.5$, directly from the symmetry considerations and the index conservation law. We now seek a periodical and smooth solution for the intermediate values of $\overline{\Delta z}$, assuming that $n_{xx}(\overline{\Delta z})$ can be expressed as:

$$n_{xx}(\overline{\Delta z}) = A + B\cos(2\pi\overline{\Delta z}), \qquad (3)$$

so that using Eq. (2) the $n_{zz}(\Delta z)$ component is given by:

$$n_{zz}(\Delta z) = n_{\parallel}n_{\perp}[A + B\cos(2\pi\overline{\Delta z})]^{-1}, \qquad (4)$$

with $A = 0.5\left(n_{\parallel} + \sqrt{n_{\parallel}n_{\perp}}\right)$ and $B = 0.5\left(n_{\parallel} - \sqrt{n_{\parallel}n_{\perp}}\right)$ obtained from the boundary cases $\overline{\Delta z} = 0$ and $\overline{\Delta z} = 0.5$. Figure 1(c) shows the calculated components of the tensor by using Eq. (3) and Eq. (4) (solid lines). Simulation of the structure with a plane wave expansion tool[38] (Fig. 1(c), dots) shows an excellent agreement with the model – see the methods section for further details on the simulation approach. The simulations also confirm that the n_{yy} component is not affected by the shifting, which can be intuitively understood by noting that the *y*-polarized electric field is always parallel to the interfaces.

We can draw several important conclusions from the results presented in Fig. 1(c). First, the bricked SWG effectively behaves as biaxial crystal, i.e. $n_{yy} \geq n_{xx} \geq n_{zz}$. Second, the properties of this crystal can be controlled by changing the shift Δz, while maintaining a rectangular, Manhattan-like geometry and constant duty-cycles. Third, for a light wave propagating along the *z*-axis, the *k*-vector magnitude, $k(\overline{\Delta z}) = \frac{2\pi}{\lambda} n_{xx}(\overline{\Delta z})$, decreases as the shift is increased. This implies that compared to a conventional subwavelength grating, for a given period Λ_z, the Bragg resonance wavelength (λ_{B}) is shortened:

$$\lambda_{\mathrm{B}}(\overline{\Delta z}) = \lambda_{\mathrm{B}}(0)\frac{n_{xx}(\overline{\Delta z})}{n_{xx}(0)}. \qquad (5)$$

As we will show in the next section, Eq. (5) accurately predicts the foreshortening of the Bragg wavelength not only in the infinitely extended metamaterial but also when including mode confinement effect in a planar waveguide geometry.

Waveguiding in the bricked SWG metamaterial. We now examine the waveguide properties of the bricked SWG metamaterial, considering the general case of a multimode waveguide. We consider two bricked SWG waveguides both with a core width $w = 3.3$ µm, a core thickness $H = 0.22$ µm and duty-cycles of 50% in both the x and z directions (i.e., yielding the largest pixel dimensions), with different periods. In the first waveguide the periods are set to $\Lambda_x = \Lambda_z = 250$ nm while in the second waveguide we choose $\Lambda_x = \Lambda_z = 300$ nm, so the Bragg wavelength is longer for the latter. In Figures 2(a) and 2(b) we show the effective index dispersion of the fundamental TE and TM Floquet-Bloch modes for different shifting values ranging from $\overline{\Delta z} = 0$ to $\overline{\Delta z} = 0.5$ for the $\Lambda = 250$ nm and $\Lambda = 300$ nm waveguides, respectively, calculated via 3D-FDTD simulations – see the methods section for further details on the simulation approach. The solid lines in Fig. 2 confirm that the effective index and the dispersion of the fundamental TE (x-polarized) mode are reduced as the shifting increases. This is achieved without significantly affecting the fundamental TM (y-polarized) mode (dotted lines), thus also providing control over modal birefringence. The effect of the shift on the Bragg wavelength is particularly noticeable in Fig. 2(b). Without a shift ($\overline{\Delta z} = 0$) the waveguide with the 300 nm period, cannot effectively guide the wavelengths near $\lambda_0 = 1.55$ µm because it operates in the bandgap. By using Eq. (5), the Bragg wavelength shortening can be accurately estimated, as shown in Fig. 2(b) with a dot for each shift. This shortening of the Bragg wavelength is fundamental to achieving the desired metamaterial properties with a simple waveguide geometry with substantially increased pixel dimensions that enable wafer-scale fabrication.

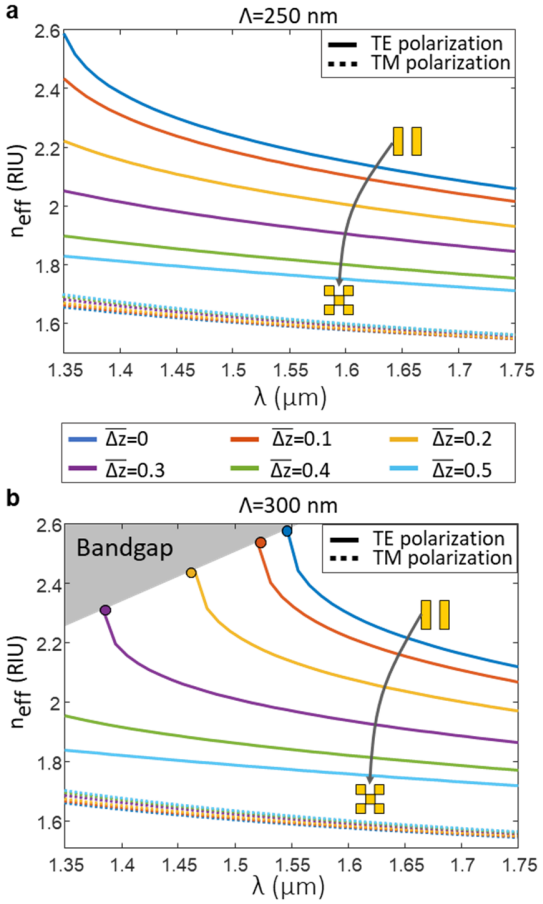

Fig. 2. Effective index dispersion of the fundamental TE and TM Floquet-Bloch modes of a 220-nm-thick bricked SWG waveguide with a width $w = 3.3$ µm, a 50% duty cycle in both directions and with periods, Λ_x and Λ_z set to (a) 250 nm (b) 300 nm. As the shift is increased the bandgap moves to shorter wavelengths – equivalently, subwavelength operation is achieved with larger pixel dimensions. The Bragg wavelength predicted by using Eq. (5) is shown with a dot for each shifting, achieving a simple but accurate approximation requiring only the simulation of the non-shifted topology. Furthermore, the modal birefringence can be precisely controlled: as the shift increases, the effective index of the fundamental TE mode is significantly reduced, while the fundamental TM mode is virtually unaffected.

Ultra-broadband beam splitter with large pixel dimensions. Ultra-broadband operation is one of the key benefits enabled by state-of-the-art SWG metamaterials[19,20,27] and is achieved by tuning the period of the structure to achieve the optimum metamaterial dispersion. However, the resulting fabrication resolutions can often be less than 100 nm, posing fabrication challenges hampering wafer-scale production of the chips. For example, an ultra-broadband multimode interferometer (MMI) demonstrated in Ref.[19] requires a period of 190 nm, resulting in gap sizes of 95 nm; in Ref.[27] a polarization beam splitter with bandwidth over 200 nm is reported, but requires 250 nm period and 65 nm fabrication resolution. Our bricked SWGs offer an advantageous solution allowing engineering of optical metamaterial properties for substantially longer grating periods with correspondingly increased fabrication resolution. To show this capability, we design two broadband 2×2 MMI couplers with SWG periods equal to $\Lambda_z = 250$ nm and $\Lambda_z = 300$ nm. For broadband operation these devices require a wavelength independent beat length of the two lowest order modes of the multimode region, defined as[39]:

$$L_\pi(\lambda) = \frac{\lambda}{2(n_{\text{eff1}} - n_{\text{eff2}})}, \tag{6}$$

where n_{eff1} and n_{eff2} are the effective indices of the first and second TE Floquet-Bloch modes [see Fig. 3(a)]. In Fig. 3(b) and (c) we show the beat lengths with different shifts ranging from $\overline{\Delta z} = 0$ to $\overline{\Delta z} = 0.5$, for the $\Lambda_z = 250$ nm and $\Lambda_z = 300$ nm structures, respectively. It is observed that in both cases an almost flat beat length can be achieved with the bricked SWG structure. Importantly, at the central wavelength of 1.55 µm the $\Lambda_z = 300$ nm structure is in the bandgap when no shift is applied, and metamaterial operation allowing mode propagation is only enabled as the shift is increased.

To control the modal excitation in the multimode waveguide, the input waveguides are tapered as shown in Fig. 4(a). The tapers are divided in two parts. The first section converts the homogeneous waveguide into a conventional SWG waveguide ($\Delta z = 0$). In the second part, the required shift is gradually introduced while widening the waveguide to the input width w_a. This two-step transition is required to circumvent the Bragg regime during the transition to wider input waveguides.

The figures of merit used in the design of the MMI are the Excess Loss (EL) and the Imbalance (IB), defined as:

$$\text{EL} = -10\log\left(|S_{41}|^2 + |S_{31}|^2\right), \tag{7}$$

$$\text{IB} = 10\log\left(|S_{41}|^2/|S_{31}|^2\right), \tag{8}$$

where S_{31} and S_{41} are the scattering parameters which relate the power in the fundamental mode of the output waveguides with the power in the fundamental mode of the input port. The optimum shift for each design is fine-tuned with 3D-FDTD simulations of the full device, resulting in the optimum dimensions summarized in Table 1 (see the methods section for further details on the simulation approach). In Fig. 3(a) we show the field propagation along the MMI for the 300 nm pitch device. In Figs. 3(d) and 3(e) we show the calculated excess loss and imbalance of the optimized devices. Both designs show an ultra-broad

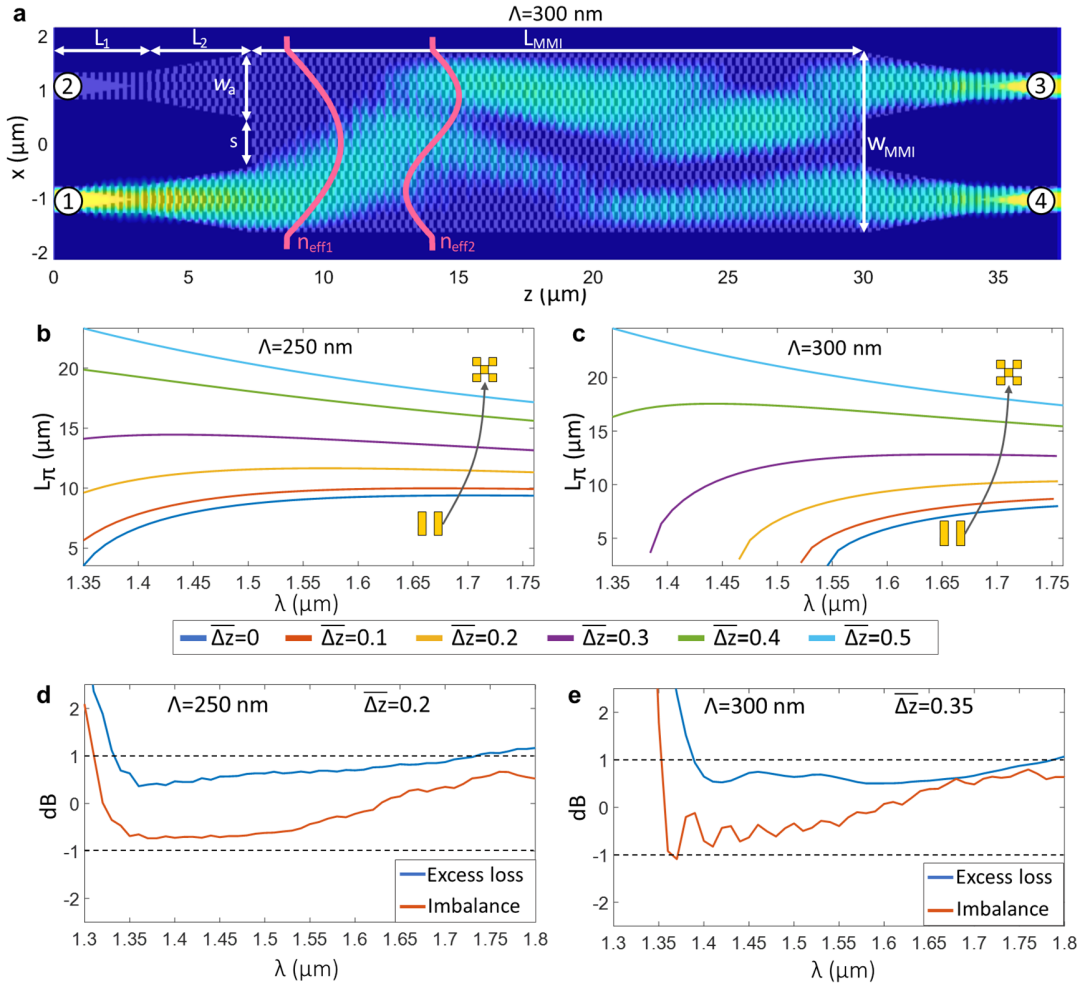

Fig. 3. (a) Simulated magnetic field propagation along the $\Lambda_z = 300$ nm bricked SWG based MMI design $|H_y|$. (b), (c) Fundamental and first order mode beat length dispersion of the TE polarization for the waveguide with (b), $\Lambda_z = 250$ nm and (c) $\Lambda_z = 300$ nm, with the shifting ranging from $\overline{\Delta z} = 0$ to $\overline{\Delta z} = 0.5$ (d), (e). Simulated excess loss (blue line) and imbalance (red line) of the optimized bricked SWG MMIs with a period of (d) $\Lambda = 250$ nm and (e) $\Lambda = 300$ nm. In both cases a 400 nm 1-dB-bandwidth is covered, from 1330 nm to 1730 nm (d), and from 1380 nm to 1780 nm (e).

bandwidth of 400 nm for an EL and IB lower than 1 dB with back reflections less than 16 dB over the full design bandwidth.

To experimentally demonstrate our brick SWG design strategy, the devices were fabricated in a commercial silicon facility using e-beam patterning and experimentally characterized (see methods section for details). Scanning electron micrographs of the devices are shown in Fig. 4(a)-(c), with slight rounding of the rectangular geometry. As shown in Fig. 4(d)-(e) the rounding had no significant impact on the performance of the devices, which both achieve EL and IB below 1 dB over the full 140 nm bandwidth of our laser. To the best of our knowledge this is the first time such outstanding performance is achieved with this large pixel sizes of 125 nm and 150 nm.

Table 1. Geometrical parameters of the bricked SWG MMIs.

Parameter	250 nm pitch design	300 nm pitch design
Silicon thickness (H)	220 nm	
MMI width (w_{MMI})	3.3 μm	
MMI length (L_{MMI})	16.5 μm	22.5 μm
Input width (w_a)	1.2 μm	
Si wire to SWG taper (L_1)	2.5 μm	3 μm
SWG to bricked SWG taper (L_2)	3.75 μm	4.5 μm
Input separation (s)	0.9 μm	
Period z (Λ_z)	250 nm	300 nm
Period x (Λ_x)	250 nm	300 nm
Shifting ($\overline{\Delta z}$)	0.2	0.35
Duty cycle z (DC_z)	50%	
Duty cycle x (DC_x)	50%	

Discussion

In this work we have demonstrated bricked SWG structures, a novel metamaterial topology that enables full lithographic control of permittivity tensor. The proposed topology relaxes the period limitations of traditional SWGs resulting in greater pixel dimensions which opens a new path towards wafer-scale fabrication of nanophotonic devices incorporating on-chip metamaterials. We have developed an analytical model that accurately predicts the behavior of the structure and have experimentally demonstrated a proof-of-concept 2×2 MMI nanophotonic coupler with bricked SWG metamaterial. Ultra-broad design bandwidth of 400 nm was confirmed by 3D FDTD simulations while our measurements reveal state-of-the-art performance over the full 140 nm bandwidth of our tunable laser, with pixel size dimensions as large as 150 × 150 nm^2. We believe that the unique advantages of bricked SWG topology will not only enable new silicon photonic devices with exceptional performance, but more importantly, will likely make the benefits of on-chip metamaterials available to the wider silicon photonics industry.

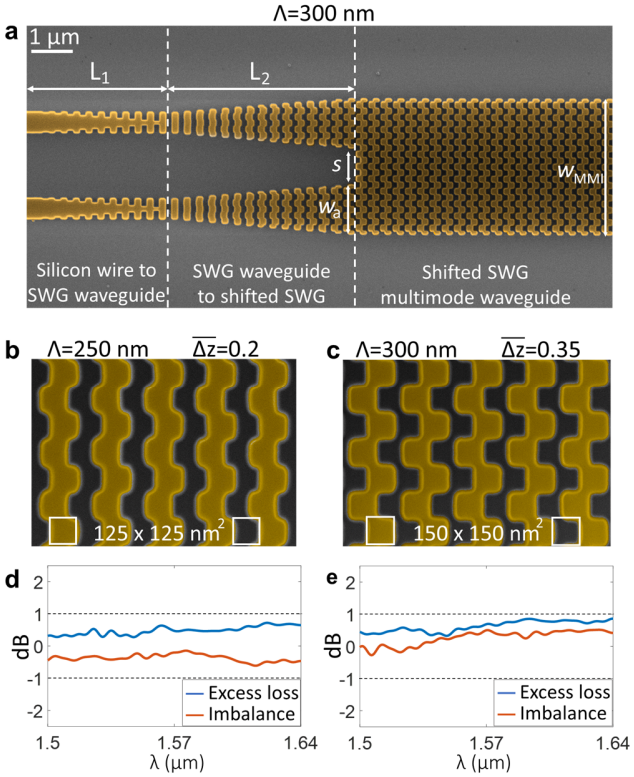

Fig. 4 a) Scanning electron microscope (SEM) images of the input section of the bricked SWG MMI; $\Lambda_z = 300$ nm. Three different sections are shown: i) Transition from a silicon wire to a conventional SWG structure. ii) Transition from a conventional SWG structure to a bricked SWG topology. iii) Multimode bricked SWG waveguide. (b), (c) SEM image of the multimode region of the (b) $\Lambda = 250$ nm and (c) $\Lambda = 300$ nm structures. The square area of the silicon segments and the gaps in between is maintained constant independently of the shift $\overline{\Delta z}$ in both cases. (d), (e) Measured excess loss and imbalance for the (d) $\Lambda = 250$ nm and (e) $\Lambda = 300$ nm structures. In both cases the measured 1 dB bandwidth is limited to the 140 nm bandwidth of our setup.

Methods

Simulation of the permittivity tensor components of a bricked subwavelength grating. The simulations of the permittivity tensor components shown in Fig. 1(c) are performed with a 2D plane wave expansion software for photonic band structures[38]. For these simulations we consider a 2D period of a bricked SWG, with periodicities $\Lambda_x = \Lambda_z = 0.1$ μm and duty cycles $DC_x = DC_z = 50\%$ for the *x*- and *z*-axis, respectively, with the shifts $\overline{\Delta z}$ ranging from 0 to 0.5 [see Fig. 1(c) insets]. The material refractive indexes of silicon and silica are $n_{Si} = 3.476$ and $n_{SiO2} = 1.444$ at a central wavelength $\lambda = 1.55$ μm. The n_{xx} and n_{yy} components are calculated as the effective index of the plane waves propagating along the *z* direction polarized in the *x*- and the *y*-axis, respectively. The n_{zz} component is calculated as the effective index of the plane wave propagating along the *x* direction polarized in the *z*-axis. The single period is meshed with 64 points in each direction, hence a grid with $64^2 = 4096$ points, which is the number of the plane waves used in the expansion algorithm.

Simulation of the effective indices of the bricked subwavelength grating waveguides. The effective index simulation of the bricked subwavelength waveguides shown in Fig. 2 and the beat length simulations presented in Fig. 3(b) and (c) are performed with a 3D finite-difference time-domain (FDTD) software for photonic structures[40]. For these simulations we consider a single period of the bricked SWG waveguide with a height $H = 220$ nm and a width $w_{MMI} = 3.3$ μm, with periodicities $\Lambda_x = 250$ nm and $\Lambda_z = 250$ nm for the first design and $\Lambda_x = 300$ nm and $\Lambda_z = 300$ nm for the second design. In both cases the duty cycles are $DC_x = DC_z = 0.5$, with the shift $\overline{\Delta z}$ ranging from 0 to 0.5. The materials are silicon for the waveguide core and silica for the upper and bottom claddings, with refractive indices $n_{Si} = 3.476$ and $n_{SiO2} = 1.444$ at a central wavelength $\lambda = 1.55$ μm. The simulation mesh is 10 nm in each dimension. To calculate the effective index with 3D-FDTD simulations we use periodic boundary conditions in the propagation direction planes $z = 0$ and $z = \Lambda_z$, defining the *k*-vector in that direction by setting the phase shift, ϕ, between these two planes. The structure is excited with a spatial and temporal Gaussian-like beam, exciting the modes of the structure at multiple wavelengths. The periodic boundary conditions allow to filter the wavelengths with a phase shift delay propagation different from, ϕ, obtaining the resonant wavelength λ_r whose electric field has the specific phase shift. The effective index at this wavelength is given by $n_{eff} = \frac{\phi\lambda_r}{2\pi\Lambda}$. This process is repeated for different phase shifts until the resonant peak coincides with the operating wavelength λ_0.

Simulation of the full device. The performance of the SWG MMIs with bricked topology, shown in Figures 3(d) and 3(e), is calculated with a 3D finite-difference time-domain (FDTD) photonic simulator[40]. We consider the devices described in Table 1, exciting the structures through the port 1 with its fundamental mode. The temporal excitation is chosen to cover full operational bandwidth. The scattering parameters S_{31} and S_{41} are calculated as the overlap integral between the mode of the output ports and the simulated field. The simulation grid is set to 10 nm in x- and z-axis and 20 nm in the y axis to properly mesh the periodic structure.

Device fabrication. The devices have been fabricated in an open access multi-project wafer with a 100 keV electron beam lithography technology[41] and the Inductively Coupled Reactive Ion Etching (ICP-RIE) process. After the device fabrication a 2.2 μm cladding SiO_2 layer is deposited by a plasma-enhanced chemical vapour deposition (PECVD) process. Finally, the chip facets are defined with a deep-etch process.

Device measurements. To characterize the fabricated devices, a custom-build test setup was used. A tunable laser (Agilent 81600B) injects the light into a polarization maintainer fiber (PMF) mounted into a rotatory stage. This fiber, together with a Glan-Thompson polarizer at the output stage, sets the desired horizontal (TE) polarization. The light is then injected into the chip, guiding the light to device under test, which splits the power into both output ports. A microscope objective, placed at the chip output, focus the light onto a photodetector (818-IR). By measuring both output ports the imbalance can be directly obtained using Eq. (8). The insertion loss measurements are obtained by comparison with a reference waveguide to cancel our system losses.

REFERENCES

1. Marin-Palomo, P. *et al.* Microresonator-based solitons for massively parallel coherent optical communications. *Nature* **546**, 274–279 (2017).

2. Wang, J. *et al.* Multidimensional quantum entanglement with large-scale integrated optics. *Science.* **360**, 285–291 (2018).

3. Llewellyn, D. *et al.* Chip-to-chip quantum teleportation and multi-photon entanglement in silicon. *Nat. Phys.* **16**, 148–153 (2020).

4. Tait, A. N. *et al.* Neuromorphic photonic networks using silicon photonic weight banks. *Sci. Rep.* **7**, 1-10 (2017).

5. Shen, Y. *et al.* Deep learning with coherent nanophotonic circuits. *Nat. Photonics* **11**, 441–446 (2017).

6. Sun, C. *et al.* Single-chip microprocessor that communicates directly using light. *Nature* **528**, 534–538 (2015).

7. Atabaki, A. H. *et al.* Integrating photonics with silicon nanoelectronics for the next generation of systems on a chip. *Nature* **556**, 349–354 (2018).

8. Miller, S. A. *et al.* Large-scale optical phased array using a low-power multi-pass silicon photonic platform. *Optica* **7**, 3-6

(2020).

9. Obrzud, E. *et al.* A microphotonic astrocomb. *Nat. Photonics* **13**, 31–35 (2019).

10. Fernández Gavela, A., Grajales García, D., Ramirez, J. & Lechuga, L. Last Advances in Silicon-Based Optical Biosensors. *Sensors* **16**, 285 (2016).

11. Giewont, K. *et al.* 300-mm Monolithic Silicon Photonics Foundry Technology. *IEEE J. Sel. Top. Quantum Electron.* **25**, 1–11 (2019).

12. Szelag, B. *et al.* Hybrid III–V/Silicon Technology for Laser Integration on a 200-mm Fully CMOS-Compatible Silicon Photonics Platform. *IEEE J. Sel. Top. Quantum Electron.* **25**, 1–10 (2019).

13. Cheben, P., Xu, D.-X., Janz, S. & Densmore, A. Subwavelength waveguide grating for mode conversion and light coupling in integrated optics. *Opt. Express* **14**, 4695–4702 (2006).

14. Cheben, P. *et al.* Refractive index engineering with subwavelength gratings for efficient microphotonic couplers and planar waveguide multiplexers. *Opt. Lett.* **35**, 2526–2528 (2010).

15. Staude, I. & Schilling, J. Metamaterial-inspired silicon nanophotonics. *Nat. Photonics* **11**, 274–284 (2017).

16. Lalanne, P. & Chavel, P. Metalenses at visible wavelengths: past, present, perspectives. *Laser Photon. Rev.* **11**, 1600295 (2017).

17. Halir, R. *et al.* Subwavelength-Grating Metamaterial Structures for Silicon Photonic Devices. *Proc. IEEE* **106**, 2144–2157 (2018).

18. Cheben, P., Halir, R., Schmid, J. H., Atwater, H. A. & Smith, D. R. Subwavelength integrated photonics. *Nature* **560**, 565–572 (2018).

19. Halir, R. *et al.* Ultra-broadband nanophotonic beamsplitter using an anisotropic sub-wavelength metamaterial. *Laser Photon. Rev.* **10**, 1039–1046 (2016).

20. González-Andrade, D. *et al.* Ultra-broadband nanophotonic phase shifter based on subwavelength metamaterial waveguides. *Photonics Res.* **8**, 359 (2020).

21. Paniagua-Domínguez, R. *et al.* A Metalens with a Near-Unity Numerical Aperture. *Nano Lett.* **18**, 2124–2132 (2018).

22. Luque-gonzález, J. M. *et al.* An Ultracompact GRIN-Lens-Based Spot Size Converter using Subwavelength Grating Metamaterials. **1900172**, 1–7 (2019).

23. Wang, Z. *et al.* On-chip wavefront shaping with dielectric metasurface. *Nat. Commun.* **10**, 3547 (2019).

24. Jahani, S. *et al.* Controlling evanescent waves using silicon photonic all-dielectric metamaterials for dense integration. *Nat. Commun.* **9**, 1893 (2018).

25. Shen, B., Wang, P., Polson, R. & Menon, R. An integrated-nanophotonics polarization beamsplitter with 2.4 × 2.4 μm2 footprint. *Nat. Photonics* **9**, 378–382 (2015).

26. Herrero-Bermello, A. *et al.* Zero-Birefringence Silicon Waveguides Based on Tilted Subwavelength Metamaterials. *IEEE Photonics J.* **11**, 1–8 (2019).

27. Xu, H., Dai, D. & Shi, Y. Ultra-Broadband and Ultra-Compact On-Chip Silicon Polarization Beam Splitter by Using Hetero-Anisotropic Metamaterials. *Laser Photon. Rev.* **13**, 1800349 (2019).

28. Xu, H., Dai, D. & Shi, Y. Anisotropic metamaterial-assisted all-silicon polarizer with 415-nm bandwidth. *Photonics Res.* **7**, 1432 (2019).

29. Luque-González, J. M. *et al.* Polarization splitting directional coupler using tilted subwavelength gratings. *Opt. Lett.* **45**, 3398 (2020).

30. Gatdula, R., Abbaslou, S., Lu, M., Stein, A. & Jiang, W. Guiding light in bent waveguide superlattices with low crosstalk. *Optica* **6**, 585 (2019).

31. Luan, E. *et al.* Enhanced Sensitivity of Subwavelength Multibox Waveguide Microring Resonator Label-Free Biosensors. *IEEE J. Sel. Top. Quantum Electron.* **25**, (2019).

32. Torrijos-Morán, L., Griol, A. & García-Rupérez, J. Experimental study of subwavelength grating bimodal waveguides as ultrasensitive interferometric sensors. *Opt. Lett.* **44**, 4702 (2019).

33. Lv, W., Liu, S., Wu, X. & Lam, E. Y. Illumination source optimization in optical lithography via derivative-free optimization. *J. Opt. Soc. Am. A* **31**, B19 (2014).

34. Luque-González, J. M. *et al.* Tilted subwavelength gratings: controlling anisotropy in metamaterial nanophotonic waveguides. *Opt. Lett.* **43**, 4691 (2018).

35. Rytov, S. M. Electromagnetic properties of a finely stratified medium. *Sov. Phys. JETP* (1956).

36. Yeh, P., Yariv, A. & Hong, C.-S. Electromagnetic propagation in periodic stratified media I General theory*. *J. Opt. Soc. Am.* **67**, 423 (1977).

37. Li, J., Miao, F., Liang, Z. & Guenneau, S. Constructing metamaterials from subwavelength pixels with constant indices product. *Opt. Express* **23**, 7140 (2015).

38. BANDSOLVE Photonic band structure software. Available at: https://www.synopsys.com/photonic-solutions/rsoft-photonic-device-tools/passive-device-bandsolve.html.

39. Soldano, L. B. & Pennings, E. C. M. Optical multi-mode interference devices based on self-imaging: principles and applications. *J. Light. Technol.* **13**, 615–627 (1995).

40. FULLWAVE FDTD Simulation Software. Available at: https://www.synopsys.com/optical-solutions/rsoft/passive-device-fullwave.html.

41. Applied Nanotools Inc. Canada. Available at: https://www.appliednt.com/nanosoi/.

Acknowledgements
We acknowledge funds from Universidad de Málaga, Ministerio de Economía y Competitividad (MINECO) (TEC2016-80718-R, PID2019-106747RB-I00), Ministerio de Educación, Cultura y Deporte (MECD) (FPU16/06762), Fondo Europeo de Desarrollo Regional—FEDER, Proyecto I+D+i en el marco del Programa Operativo FEDER Andalucía 2014-2020 (UMA18-FEDERJA-219) and Junta de Andalucía, Proyectos de Excelencia, Modalidad Retos (P18-RT-1453, P18-RT-793).

Author contributions
J.M.L.G performed the simulations of the devices and prepared the mask for the fabrication. A.O.M and R.H developed the theoretical model of the bricked SWG structures as biaxial crystal. J.H.S and P.C provided practical guidance on the fabricability of the structures. I.M.F supervised the project. J.G.W.P conceived the idea and supervised the measurements of the fabricated devices. All the authors contributed to the discussion and paper preparation.

Correspondence and requests for materials should be addressed to P.C or J.G.W.P.